



Classical 1/3 scaling of convection holds up to $Ra = 10^{15}$

Kartik P. Iyer^a, Janet D. Scheel^b, Jörg Schumacher^{a,c}, and Katepalli R. Sreenivasan^{a,d,e,f,1}

^aTandon School of Engineering, New York University, New York, NY 11201; ^bDepartment of Physics, Occidental College, Los Angeles, CA 90041; ^cDepartment of Mechanical Engineering, Technische Universität Ilmenau, D-98684 Ilmenau, Germany; ^dCourant Institute of Mathematical Sciences, New York University, New York, NY 10012; ^eDepartment of Physics, New York University, New York, NY 10012; and ^fCenter for Space Science, New York University Abu Dhabi, Abu Dhabi 129188, United Arab Emirates

Contributed by Katepalli R. Sreenivasan, February 14, 2020 (sent for review December 30, 2019; reviewed by Charles R. Doering, Gregory Falkovich, and Susanne Horn)

The global transport of heat and momentum in turbulent convection is constrained by thin thermal and viscous boundary layers at the heated and cooled boundaries of the system. This bottleneck is thought to be lifted once the boundary layers themselves become fully turbulent at very high values of the Rayleigh number Ra —the dimensionless parameter that describes the vigor of convective turbulence. Laboratory experiments in cylindrical cells for $Ra \gtrsim 10^{12}$ have reported different outcomes on the putative heat transport law. Here we show, by direct numerical simulations of three-dimensional turbulent Rayleigh–Bénard convection flows in a slender cylindrical cell of aspect ratio 1/10, that the Nusselt number—the dimensionless measure of heat transport—follows the classical power law of $Nu = (0.0525 \pm 0.006) \times Ra^{0.331 \pm 0.002}$ up to $Ra = 10^{15}$. Intermittent fluctuations in the wall stress, a blueprint of turbulence in the vicinity of the boundaries, manifest at all Ra considered here, increasing with increasing Ra , and suggest that an abrupt transition of the boundary layer to turbulence does not take place.

turbulent convection | direct numerical simulation | turbulent heat transfer

Turbulent Rayleigh–Bénard convection (RBC), triggered in a fluid layer which is uniformly heated from below and cooled from above, is considered the paradigm for buoyancy-driven turbulence reaching from stellar convection (1) via atmospheric (2) and oceanic (3) turbulence to cooling blankets in nuclear engineering (4) or the storage of renewable energy in liquid metal batteries (5). A central question in RBC is the fundamental law governing the global turbulent transport of heat and momentum across the convection layer as a function of dimensionless parameters characterizing the flow (6–11). These parameters are the Rayleigh number $Ra = g\alpha\Delta TH^3/(\nu\kappa)$, which quantifies the relative magnitude of the thermal driving to the viscous and diffusive forces of the fluid motion and is directly proportional to the temperature difference $\Delta T = T_{\text{bottom}} - T_{\text{top}}$, maintained between the top and bottom plates, and the Prandtl number $Pr = \nu/\kappa$, which is the ratio of momentum and thermal diffusivities denoted by ν and κ , respectively. Here, g , α , and H are the acceleration due to gravity, the isobaric thermal expansion coefficient, and the fluid layer height H , respectively. A third parameter is the aspect ratio $\Gamma = d/H$ for closed (cylindrical) containers of diameter d , the typical setup in which turbulent convection is studied in the laboratory. For Rayleigh numbers sufficiently above the onset value of $Ra \gg Ra_c = 1,708$, the fluid flow develops thin thermal and viscous boundary layers at the top and bottom walls that sandwich a turbulent bulk layer with a well-mixed temperature of $T \simeq T_{\text{bottom}} - \Delta T/2$. The heat which is supplied at the bottom has to be transmitted through the boundary layers that act as bottlenecks, which are thought to be removed when the thin boundary layers become turbulent themselves (12, 13), leading, potentially, to the so-called “ultimate” state of turbulent convection. It is not known precisely at what Rayleigh numbers this transition is presumed to occur, but high-Rayleigh-number laboratory experiments in cylindrical cells (14–20) have

reported different outcomes on the turbulent transport law for $Ra \gtrsim 10^{12}$.

In this paper, we assess the laws of turbulent heat and momentum transport in RBC by direct numerical simulations (DNS) of the Boussinesq equations that couple the (turbulent) velocity field $u_i(x, y, z, t)$ with the temperature field $T(x, y, z, t)$, with $i = x, y, z$. We cover Rayleigh numbers in the range $10^8 \leq Ra \leq 10^{15}$ at the Prandtl number Pr held fixed at unity, such that the momentum and thermal boundary layers have similar thicknesses and scale the same way with Ra . We used massively parallel computations that apply the spectral element method (21, 22) and experimented with increasing grid resolutions and finer time steps until the veracity of the data was established (see *SI Appendix* and Table 1 for more details). Despite the heftiness of the computations, our goal of pushing toward the highest possible Rayleigh numbers meant that we had to compromise on the aspect ratio Γ , which we held at 1/10. Even for this low aspect ratio, the boundary layer thickness at the highest Ra is about 1/1,000 the diameter of the cylindrical cell, and the heat transport results agree closely, where they overlap, with previous results for aspect ratio unity, obtained using the same numerical methods (23). A comparison with the experimental data of Niemela and Sreenivasan (15) at $\Gamma = 1$ also shows that the two are quite close.

Significance

The heat transport law in turbulent convection remains central to current research in the field. Our present knowledge of the heat transport law for $Ra > 10^{12}$ is inconclusive, where the Rayleigh number Ra is a measure of the strength of convection. Massively parallel simulations of the three-dimensional convection have progressed to $Ra = 10^{15}$ in slender cells. We resolve velocity gradients inside thin boundary layers and show that the turbulent heat transport continues to follow the classical 1/3 scaling law with no transition to the so-called “ultimate” state that is variously argued to have 1/2 scaling. Our work suggests that the boundary layers remain marginally stable and continue to act as the bottleneck for global heat transport.

Author contributions: J.D.S., J.S., and K.R.S. designed research; K.P.I., J.D.S., and J.S. performed research; K.P.I., J.D.S., J.S., and K.R.S. analyzed data; and J.S. and K.R.S. wrote the paper.

Reviewers: C.R.D., University of Michigan, Ann Arbor; G.F., Weizmann Institute of Science; and S.H., Coventry University.

The authors declare no competing interest.

This open access article is distributed under [Creative Commons Attribution-NonCommercial-NoDerivatives License 4.0 \(CC BY-NC-ND\)](https://creativecommons.org/licenses/by-nc-nd/4.0/).

See [online](#) for related content such as Commentaries.

¹To whom correspondence may be addressed. Email: katepalli.sreenivasan@nyu.edu.

This article contains supporting information online at <https://www.pnas.org/lookup/suppl/doi:10.1073/pnas.1922794117/-DCSupplemental>.

First published March 25, 2020.

Table 1. Summary of spectral element simulation parameters

Ra	Nu	Re	t	M	N	N_e
10^8	29.94 ± 0.04	601 ± 1	245	46	3	19,200
10^9	58 ± 10	$1,920 \pm 14$	396	89	5	19,200
10^{10}	107 ± 11	$5,570 \pm 50$	419	104	5	19,200
10^{11}	229 ± 13	$17,000 \pm 200$	136	58	9	19,200
10^{12}	503 ± 25	$52,500 \pm 2,000$	58	99	11	537,600
10^{13}	$1,075 \pm 44$	$133,000 \pm 2,000$	24	83	13	925,200
10^{14}	$2,228 \pm 100$	$410,000 \pm 10,000$	14	83	11	17,145,600
10^{15}	$4,845 \pm 200$	$1,094,000 \pm 10,000$	7	82	11	17,145,600

The table lists the Rayleigh number Ra, the Nusselt number Nu obtained from heat flux through the top/bottom plates, the Reynolds number Re, the total simulation time t in free-fall time units t_f , the number of three-dimensional simulation snapshots M , the polynomial order N of the Lagrangian interpolation polynomials for each of the three space directions, and the total number of spectral elements N_e . This results in a total number of mesh cells of $N_e \times N^3$ which results in more than 2.2×10^{10} mesh cells for the biggest simulation run. The Prandtl number is unity for all cases. Simulation time t is the time in a statistically stationary state at the highest spectral resolution in each run. It is this time that is used for the statistical analysis of the main text.

Global Heat and Momentum Transfer

Our principal results are shown in Fig. 1. In Fig. 1 A and B, we plot the Nusselt number Nu against the Rayleigh number Ra. The Nusselt number is obtained for each integration time step as an average of the vertical diffusive heat current $\kappa \partial T / \partial z$ taken at the bottom and top walls over the cell cross-section $A = \pi d^2 / 4$. The data at bottom and top walls are subsequently combined in a time average to give Nu and the associated error bars. In SI Appendix, we compare this method of determination with a second, which is based on the combined volume-time average of the sum of the convective and diffusive heat currents, and find very good consistency. The earlier simulation results at lower Rayleigh number for $Pr = 0.7$ and $\Gamma = 1$ (23) are also shown; together, the data cover almost 10 orders of magnitude in Ra with an overlap of the two records for $10^8 \leq Ra \leq 10^{10}$. Fig. 1A shows that a good power-law scaling exists for $10^{10} \leq Ra \leq 10^{15}$, with the exponent given by 0.331 ± 0.002 . For lower Ra, the exponent has a smaller value of 0.29 ± 0.01 , as is well known from past considerations (11) and which is close to $2/7$ (8). These data are in good agreement with the experimentally measured Nusselt numbers in cryogenic helium (15), as shown in SI Appendix. Recent experiments by de Wit et al. (24) in a water column at $\Gamma = 1/10$ for $10^{10} < Ra < 10^{14}$ report $Nu = 0.11 \times Ra^{0.308 \pm 0.005}$.

Fig. 1. Global scaling laws of turbulent transport. (A) Turbulent heat transport law $Nu(Ra)$ for two datasets on log-log coordinates. The present data (open circles) are for $Pr = 1$ and $\Gamma = 0.1$ for $10^8 \leq Ra \leq 10^{15}$. Open squares representing DNS at $Pr = 0.7$ and $\Gamma = 1$ for $3 \times 10^5 \leq Ra \leq 10^{10}$ are taken from ref. 23. Also added is the power-law fit of $Nu = (0.0525 \pm 0.006) \times Ra^{0.331 \pm 0.002}$ which is obtained for $10^{10} \leq Ra \leq 10^{15}$. (B) Linear-log plot of the data of A, displayed in the form of compensated classical power law of $1/3$ slope, with error bars computed from the standard deviation of the time series $Nu(t)$, obtained at $\bar{z} = z/H = 0$ (bottom) and $\bar{z} = 1$ (top). The plot shows that the power-law exponent is smaller (0.29 ± 0.01) for $Ra \leq 10^9$ and is $1/3$ in the high-Ra range, with no tendency to a larger slope as would be required of the possible progression to the ultimate state. The dashed line corresponds to prefactor 0.0525, in close agreement with the classical prediction of 0.073 (6, 7). (C) Compensated power-law plot of the turbulent momentum transport law $Re(Ra)$. A fit over the same Rayleigh number range as in B gives $Re = (0.1555 \pm 0.006) \times Ra^{0.458 \pm 0.006}$. Symbols mean the same in A–C.

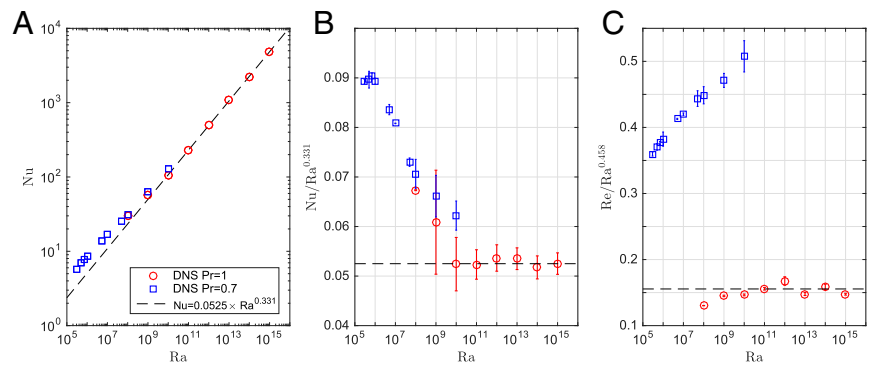


Fig. 1B replots the Nusselt number compensated by the scaling, $Nu/Ra^{0.331}$. The classical $1/3$ scaling is satisfied over five decades of Ra starting from 10^{10} . We stress that the prefactor of 0.0525 ± 0.006 is also close to the theoretical prediction of 0.073 (6, 7) based on the assumption that marginally stable boundary layers maximize the heat transport. The present Nusselt numbers match, within error bars, with the earlier data of ref. 23 for the cell aspect ratio of unity, suggesting that the present aspect ratio, although small, is not too small for purposes of heat transport (see discussion of Fig. 2).

The turbulent momentum transport is given by the Reynolds number $Re = \tilde{u}_{rms} \sqrt{Ra/Pr}$ (see SI Appendix for details). Throughout this work, tildes denote dimensionless physical quantities expressed in characteristic units composed of height H , free-fall velocity $U_f = \sqrt{g\alpha\Delta TH}$, and/or the wall-to-wall temperature difference ΔT . Times are thus given in units of the free-fall time $t_f = H/U_f$. Fig. 1C shows the compensated plot $Re/Ra^{0.458}$ for the two sets of data. The Reynolds number scaling in the slender cell is given by $Re = (0.1555 \pm 0.006) \times Ra^{0.458 \pm 0.006}$ for $Ra \geq 10^{10}$, with no apparent tendency toward a qualitative change toward the highest values of Ra. For $\Gamma = 1$, this same power law has an exponent of 0.49 ± 0.01 (23); in the overlapping region of Ra, the magnitudes are larger by a factor of 3 to 5. We shall discuss this result toward the end. Note that a scaling $Re(Ra)$ with an exponent of $1/2$ does not necessarily herald the “ultimate” convection state.

Boundary Layer Structure

Fig. 2 illustrates the complex structure of the turbulent fields inside the thermal boundary layers for three values of the Rayleigh number. The mean thickness of the thermal boundary layer is given by $\delta_T = H/(2Nu)$. Fig. 2A–F shows horizontal cuts through the temperature field \tilde{T} and the velocity field $(\tilde{u}_x, \tilde{u}_y, 0)$ at $z = \delta_T/2$. Fig. 2G–I shows contours of the magnitude of the wall shear stress field at the bottom plate, defined in RBC for $Pr = 1$ in characteristic units as

$$\tilde{\tau}_w(\tilde{x}, \tilde{y}, \tilde{z} = 0) = \sqrt{\frac{1}{Ra} \left[\left(\frac{\partial \tilde{u}_x}{\partial \tilde{z}} \right)^2 + \left(\frac{\partial \tilde{u}_y}{\partial \tilde{z}} \right)^2 \right]}. \quad [1]$$

For all three datasets, the fields develop ever-finer structures and filaments as the Rayleigh number increases from 10^{11} to 10^{15} . The wall shear stress magnitude (Fig. 2, G–I) and velocity field streamlines (Fig. 2, D–F) illustrate the complexity of interactions of the flow near the bottom plate with the fine ridges of thermal plumes (Fig. 2, A–C).

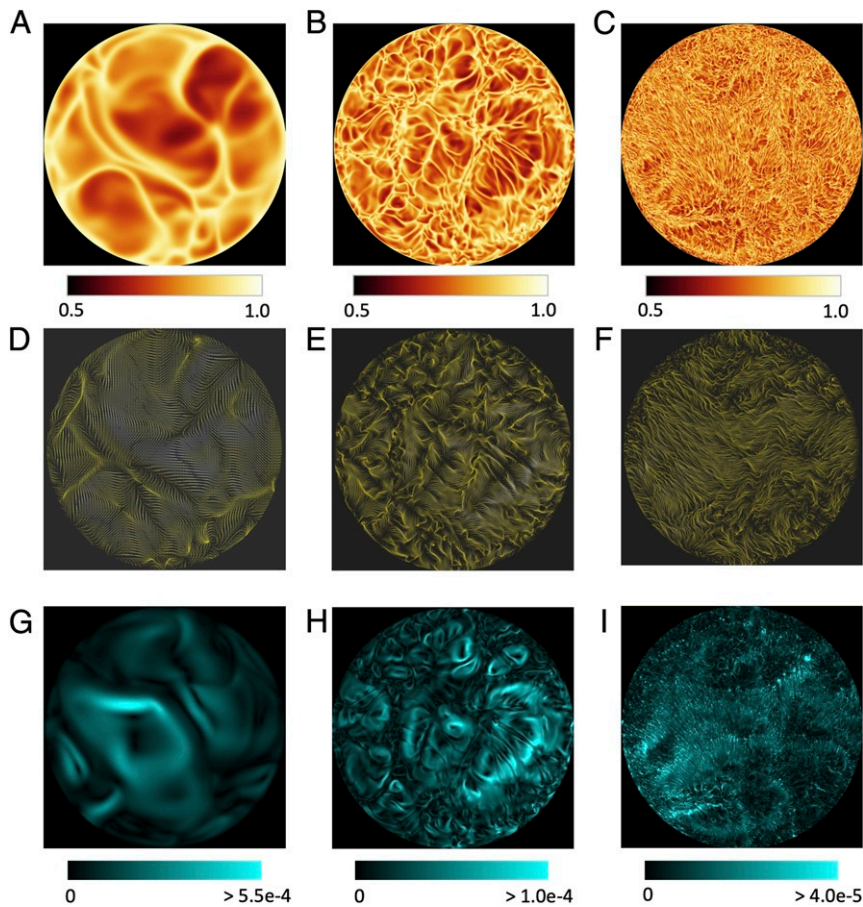
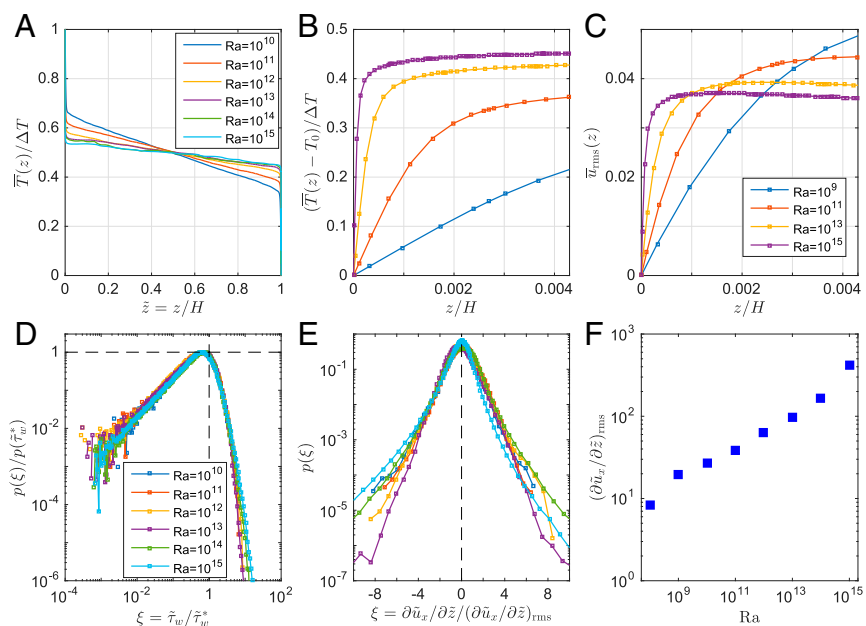


Fig. 2. Convection flow inside the boundary layers. Snapshots of the temperature and velocity fields are displayed for three different Rayleigh numbers. (A–C) Temperature field at a Rayleigh number of (A) $Ra = 10^{11}$ in a horizontal plane at $z = 0.001H$, (B) $Ra = 10^{13}$ for $z = 0.0002H$, and (C) $Ra = 10^{15}$ for $z = 0.00005H$. The heights of these planes correspond to half of the thermal boundary layer thickness, $\delta_T/2$. The temperature range is given by the color bar below each panel. (D–F) Streamlines of the velocity field which is projected onto the cutting plane, that is, $u_z = 0$ shown at (D) $Ra = 10^{11}$, (E) $Ra = 10^{13}$, and (F) $Ra = 10^{15}$. The distance from the bottom wall is the same as in the corresponding temperature plots. (G–I) Contour plot of the wall shear stress magnitude $\bar{\tau}_w$ for $z = 0$ at (G) $Ra = 10^{11}$, (H) $Ra = 10^{13}$, and (I) $Ra = 10^{15}$.

Fig. 3 shows the average behaviors of the thermal and the mean-square velocity fields. Fig. 3A shows the mean temperature profiles at various Ra , Fig. 3B shows the corresponding boundary

layer behavior, and Fig. 3C shows the root-mean-square of the velocity fluctuations. They are very similar in behavior to those in higher aspect ratios.

Fig. 3. Statistical analysis within the boundary layer. (A) Mean dimensionless temperature profiles $\bar{T}(z)/\Delta T$ versus cell height $\bar{z} = z/H$. The profiles are obtained as averages over the circular cross-section at each z and time. (B) Zoom-in of the near-wall region. Data are the same as in A, but replotted now as $(\bar{T}(z) - T_0)/\Delta T$ with $T_0 = T(0)$. An additional arithmetic average over both halves of the mean profiles is performed to improve statistics. This is possible due to the up-down symmetry in the Boussinesq approximation with respect to the midplane. The range displayed here corresponds to $0 \leq z \leq \delta_T/2$, with the mean thermal boundary layer thickness δ_T taken at $Ra = 10^9$. (C) Same zoom of the mean velocity fluctuation profiles $\bar{u}_{rms}(z)$ in units of the free-fall velocity U_f . The root-mean-square value is determined with respect to all three velocity components, and profiles are obtained in the same way as in B. The legend is the same for B and C. (D) Probability density function (PDF) of the dimensionless wall shear stress magnitude given by Eq. 1. In each dataset, the argument is rescaled by the corresponding stress value of the maximum of the PDF, $\bar{\tau}_w^*$. All PDFs are also normalized to unity. (E) PDF of the single partial derivative $\partial \bar{u}_x / \partial \bar{z}$ at $\bar{z} = 0, 1$ given in units of the corresponding root-mean-square value. The legend is the same as D. (F) Root-mean-square value $(\partial \bar{u}_x / \partial \bar{z})_{rms}$ versus Rayleigh number Ra . In D–F, the analysis is limited to an inner section of the plate with $\bar{r} \leq 0.03$.



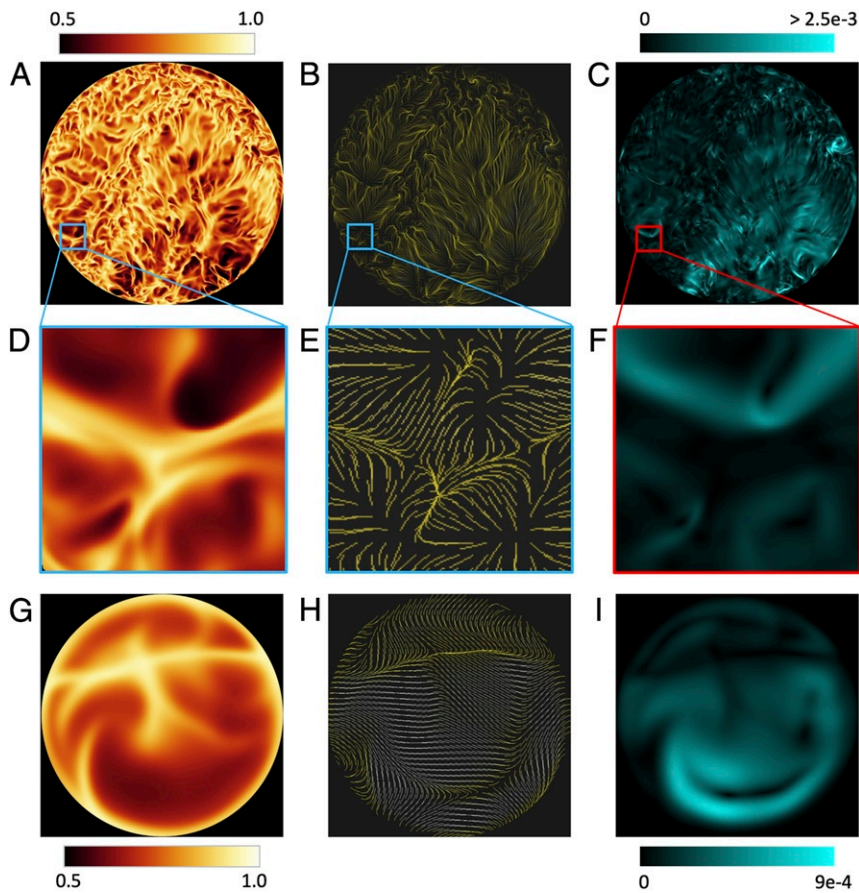


Fig. 4. Comparison of the boundary layer structure at different aspect ratios but same Rayleigh number. *A*, *D*, and *G* show temperature slices, and *B*, *E*, and *H* show the projected streamlines at $z = \delta_T/2 \approx 0.002H$. *C*, *F*, and *I* show the wall shear stress magnitude at $z = 0$ similar to Fig. 2. The data in *G–I* correspond to $Ra = 10^{10}$, $Pr = 1$, and $\Gamma = 0.1$. *A–C* and zooms in *D–F* are for $Ra = 10^{10}$, $Pr = 0.7$, but $\Gamma = 1$ (23). The zoom-up pictures with a box side length of $d = 0.1H$ show that they are very similar to the case of the lower aspect ratio.

Our conclusion, then, is that the behavior of the temperature field and the fluctuating velocity field in the present simulations is very similar to those at higher aspect ratios, essentially because the boundary layers are very thin compared to the cell diameter. This is illustrated further in Fig. 4 by a direct comparison of boundary layer snapshots at aspect ratios 1 and 1/10 at $Ra = 10^{10}$. All of the heat supplied at the bottom plate has to pass through thin boundary layers; as already stated, this bottleneck is thought to be removed when the boundary layers become fully turbulent themselves, leading to the “ultimate” state (12). However, the boundary layer dynamics in RBC is distinct from that of the canonical isothermal boundary layers in channels or over flat plates with a unidirectional mean flow (25). The boundary layer motion in RBC lumps together hotter (colder) segments of the thermal boundary layer which detach from the bottom (top) plate and rise (fall) into the well-mixed bulk, thus disrupting the near-wall fluid motion by updrafts at all Rayleigh numbers; it is also subject to plume impacts and couples to the large-scale motion in the bulk. The perturbations in the convection boundary layer are large even at moderate Rayleigh numbers, and a distinct event, such as the classical boundary layer transition to turbulence, seems unlikely in convection. This expectation is supported in Fig. 3*D*, which shows that the wall shear stress fluctuations possess no sudden changes with Ra , and that their distributions at different Ra can be collapsed very well between $Ra = 10^{10}$ and $Ra = 10^{15}$ with a linear tail for the smallest amplitudes. The vertical derivatives for a single velocity component at the plates show similar broadband behavior (Fig. 3*E*), and their relatively large root-mean-square values grow continuously (Fig. 3*F*), suggesting that the boundary layers at these fluctuation levels are already turbulent for Rayleigh numbers $\gtrsim 10^{10}$. This intrinsic reason undercuts the notion that the heat transport

would change to a different behavior at higher Rayleigh numbers. We speculate that the argument may hold for larger aspect ratios as well.

Large-Scale Flow Organization

We now return to the Reynolds number results (see Fig. 1*C* again). The difference in the momentum transport between the results for $\Gamma = 1$ (or larger aspect ratios) and the present results can be attributed to the particular large structure in the slender cylinder. Fig. 5 *A–D* displays isosurfaces of the vertical velocity component. They indicate a helical large-scale structure (similar to a barber pole) for all three Rayleigh numbers shown; indeed, this structure persists throughout the whole range of Ra starting from $Ra = 10^8$ and serves some of the same purposes as the large-scale circulation in high aspect ratio convection, in linking the bottom and top walls directly. This helical flow structure collapses sometimes, and the winding number alters, but the feature is generally robust. This can be seen clearly at $Ra = 10^{11}$, for which two views are shown. As a result of this flow, the mean temperature profile obeys a nearly linear form in the midsection, just as for higher aspect ratio cases (Fig. 3*A*). While this large-scale flow has some effect in transporting momentum, as seen by the disparity in Reynolds numbers in the overlap range between the present data and those of ref. 23, it seems to have negligible impact on the turbulent heat transport, as discussed earlier. Fig. 5 *E–H* provides horizontal cuts through the cylinder in the central region, which confirm the appearance of ever-finer vertical velocity filaments that leave the large-scale flow essentially unaffected. As far as the small-scale motion is concerned, the aspect ratio of 1/10 seems to have no obvious effect. Thus, the different large-scale flow structures in different aspect ratio cylindrical cells seem to matter for turbulent momentum

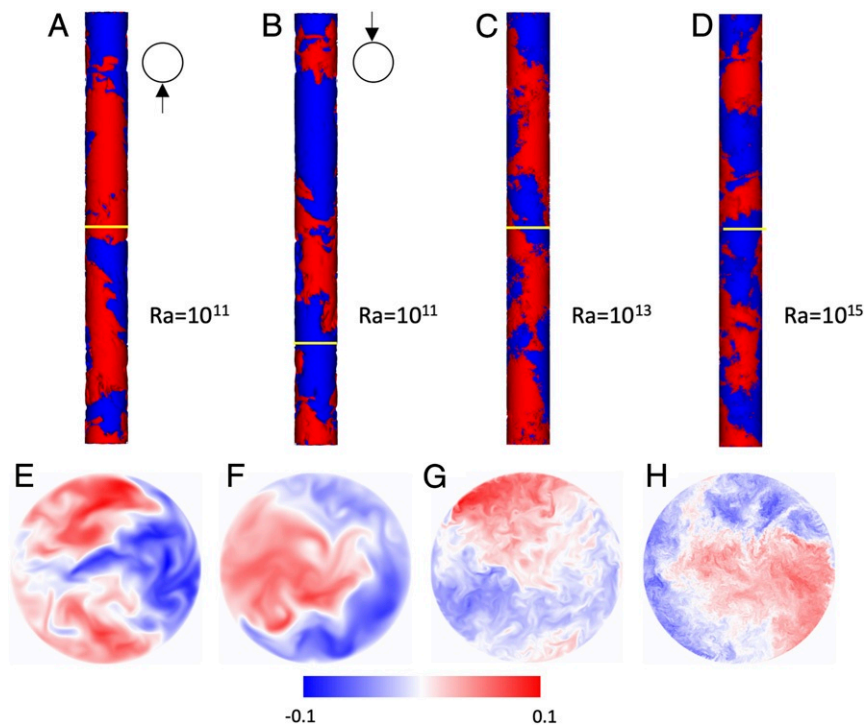


Fig. 5. Large-scale flow organization in slender cell and the increasingly small structure with increasing Ra . (A) Front view of an isosurface plot showing a snapshot of the vertical velocity field component at the levels $u_z = \pm 0.01$ (blue, negative; red, positive) at $Ra = 10^{11}$. The symbol to the right indicates the specific plan view. (B) Replot of the data with the front view rotated by 180° with respect to A in order to highlight the helical nature of the large scale. (C and D) Isosurface plots for (C) $Ra = 10^{13}$ and (D) for $Ra = 10^{15}$. (E and F) Contour plot of the vertical velocity field at $z/H = 1/2$ for $Ra = 10^{11}$, and (F) at $z/H = 1/4$ for the same snapshot. (G and H) Contour plot of the vertical velocity field at $z/H = 1/2$ for (G) $Ra = 10^{13}$ and (H) $Ra = 10^{15}$. The vertical positions of the expanded horizontal planes in E–G are highlighted by a yellow ring in each of the front views (in A–D). The three snapshots also correspond to those displayed in Fig. 2.

transport but apparently not for the small structure and the turbulent heat transport.

In conclusion, our DNS show that, at least in the low- Γ case, there is no tendency toward the “ultimate” state up to $Ra = 10^{15}$. We cannot exclude that the present large-scale flow shifts its appearance at higher Ra , or that some new heat transport law might set in. However, the fact that the boundary layers at these Rayleigh numbers are already strongly fluctuating suggests that no new state of turbulence is likely to appear, thus making it unlikely that the heat transport law will depart from the classical $1/3$ power; this is consistent with the conclusion of ref. 15 from experiments in a cell of $\Gamma = 1$.

Data Availability. Data are available upon request from the corresponding author.

ACKNOWLEDGMENTS. The present computations were enabled by an award of computer time provided by the Innovative and Novel Computational Impact on Theory and Experiment program, and used resources of the Argonne Leadership Computing Facility, which is a Department of Energy Office of Science User Facility supported under Contract DE-AC02-06CH11357. J.D.S. and J.S. are supported by the Priority Program DFG-SPP 1881 “Turbulent Superstructures” of the Deutsche Forschungsgemeinschaft. Computing resources are provided by Grant HIL12 of the John von Neumann Institute for Computing in Jülich. We thank Stefan Kerkemeier for his help in improving the code performance.

- C. Paladini et al., Large granulation cells on the surface of the giant star π^1 Gruis. *Nature* **553**, 310–312 (2018).
- A. A. Wing, K. Emanuel, C. E. Holloway, C. Muller, Convective self-aggregation in numerical simulations: A review. *Surv. Geophys.* **38**, 1173–1197 (2017).
- F. Fröb et al., Irminger Sea deep convection injects oxygen and anthropogenic carbon to the ocean interior. *Nat. Commun.* **7**, 13244 (2016).
- W. Guo, A. Ying, M.-J. Ni, M. A. Abdou, Influence of 2D and 3D convection-diffusion flow on tritium permeation in helium cooled solid breeder blanket units. *Fusion Eng. Des.* **81**, 1465–1470 (2006).
- K. Wang et al., Lithium–antimony–lead liquid metal battery for grid-level energy storage. *Nature* **514**, 348–350 (2014).
- W. V. R. Malkus, The heat transport and spectrum of thermal turbulence. *Proc. R. Soc. Lond. A* **225**, 196–212 (1954).
- E. A. Spiegel, “On the Malkus theory of turbulence” in *Mécanique de la Turbulence* (Centre National de la Recherche Scientifique, 1962), pp. 181–201.
- B. Castaing et al., Scaling of hard thermal turbulence in Rayleigh–Bénard convection. *J. Fluid Mech.* **204**, 1–30 (1989).
- E. D. Siggia, High Rayleigh number convection. *Annu. Rev. Fluid Mech.* **26**, 137–168 (1994).
- G. Ahlers, S. Großmann, D. Lohse, Heat transfer and large-scale dynamics in turbulent Rayleigh–Bénard convection. *Rev. Mod. Phys.* **81**, 503–537 (2009).
- F. Chillà, J. Schumacher, New perspectives in turbulent Rayleigh–Bénard convection. *Eur. J. Phys. E* **35**, 58 (2012).
- R. H. Kraichnan, Turbulent thermal convection at arbitrary Prandtl number. *Phys. Fluids* **5**, 1374–1389 (1962).
- E. A. Spiegel, Convection in stars. Part I. Basic Boussinesq convection. *Annu. Rev. Astron. Astrophys.* **9**, 323–352 (1971).
- J. J. Niemela, L. Skrbek, K. R. Sreenivasan, R. J. Donnelly, Turbulent convection at very high Rayleigh numbers. *Nature* **404**, 837–840 (2000).
- J. J. Niemela, K. R. Sreenivasan, Confined turbulent convection. *J. Fluid Mech.* **481**, 355–384 (2003).
- X. Chavanne, F. Chillà, B. Chabaud, B. Castaing, B. Hébral, Turbulent Rayleigh–Bénard convection in gaseous and liquid He. *Phys. Fluids* **13**, 1300–1320 (2001).
- P. Urban, V. Musilová, L. Skrbek, Efficiency of heat transfer in turbulent Rayleigh–Bénard convection. *Phys. Rev. Lett.* **107**, 014302 (2011).
- X. He, D. Funfschilling, H. Nobach, E. Bodenschatz, G. Ahlers, Transition to the ultimate state of turbulent Rayleigh–Bénard convection. *Phys. Rev. Lett.* **108**, 024502 (2012).
- C. R. Doering, S. Toppaladoddi, J. S. Wettlaufer, Absence of evidence for the ultimate regime in two-dimensional Rayleigh–Bénard convection. *Phys. Rev. Lett.* **123**, 259401 (2019).
- X. Zhu, V. Mathai, R. J. A. M. Stevens, R. Verzicco, D. Lohse, Reply to “Absence of evidence for the ultimate regime in two-dimensional Rayleigh–Bénard convection.” *Phys. Rev. Lett.* **123**, 259402 (2019).
- P. F. Fischer, An overlapping Schwarz method for spectral element solution of the incompressible Navier–Stokes equations. *J. Comput. Phys.* **133**, 84–101 (1997).
- J. D. Scheel, M. S. Emran, J. Schumacher, Resolving the fine-scale structure in turbulent Rayleigh–Bénard convection. *New J. Phys.* **15**, 113063 (2013).
- J. D. Scheel, J. Schumacher, Predicting transition ranges to fully turbulent viscous boundary layers in low Prandtl number convection flows. *Phys. Rev. Fluids* **2**, 123501 (2017).
- X. M. de Wit et al., Turbulent rotating convection confined in a slender cylinder: The sidewall circulation. *Phys. Rev. Fluids* **5**, 023502 (2020).
- I. Marusic et al., Wall-bounded turbulent flows at high Reynolds numbers: Recent advances and key issues. *Phys. Fluids* **22**, 065103 (2010).

Supplementary Information for

Classical 1/3 scaling of convection holds up to $Ra = 10^{15}$

Kartik P. Iyer, Janet D. Scheel, Jörg Schumacher and Katepalli R. Sreenivasan

Katepalli R. Sreenivasan.

E-mail: katepalli.sreenivasan@nyu.edu

This PDF file includes:

Supplementary text

Figs. S1 to S2

Table S1

References for SI reference citations

Supporting Information Text

This supplementary information provides additional figures reinforcing the main text. For the most part, the captions of the figures and the tables are self-contained.

Mathematical model - Boussinesq equations

We solve the coupled three-dimensional equations of motion for velocity field u_i and temperature field T in the Boussinesq approximation of thermal convection:

$$\frac{\partial \tilde{u}_i}{\partial \tilde{x}_i} = 0, \quad [1]$$

$$\frac{\partial \tilde{u}_i}{\partial \tilde{t}} + \tilde{u}_j \frac{\partial \tilde{u}_i}{\partial \tilde{x}_j} = -\frac{\partial \tilde{p}}{\partial \tilde{x}_i} + \sqrt{\frac{\text{Pr}}{\text{Ra}}} \frac{\partial^2 \tilde{u}_i}{\partial \tilde{x}_j^2} + \tilde{T} \delta_{i3}, \quad [2]$$

$$\frac{\partial \tilde{T}}{\partial \tilde{t}} + \tilde{u}_j \frac{\partial \tilde{T}}{\partial \tilde{x}_j} = \frac{1}{\sqrt{\text{RaPr}}} \frac{\partial^2 \tilde{T}}{\partial \tilde{x}_j^2}, \quad [3]$$

with Rayleigh number Ra and Prandtl number Pr . The indices i, j can have the values x, y, z and the tilde stands for a dimensionless variable. The Einstein summation convention is used. The equations are made dimensionless by cell height H , free-fall velocity $U_f = \sqrt{g\alpha\Delta TH}$ and the imposed temperature difference ΔT between bottom and top plates. The aspect ratio $\Gamma = d/H = 0.1$. No-slip boundary conditions for the fluid are applied at all walls, thus enforcing $\tilde{u}_i = 0$. The vertical enclosure is thermally insulated at the side wall, i.e., $\partial\tilde{T}/\partial\tilde{n} = 0$. The top and bottom plates are held at constant dimensionless temperatures $\tilde{T} = 0$ and 1 , respectively. The Prandtl number is $\text{Pr} = 1$ for all runs.

Measures of global turbulent transport

The Nusselt number Nu (and thus the turbulent heat transfer) can be computed by two different methods which are given for $\text{Pr} = 1$ in dimensionless form by

$$\text{Nu} = \langle |\partial\tilde{T}(\tilde{z})/\partial\tilde{z}| \rangle_{A,t} \quad \text{at} \quad \tilde{z} = 0, 1, \quad [4]$$

$$\text{Nu}_V \equiv 1 + \sqrt{\text{Ra}} \langle \tilde{u}_z \tilde{T} \rangle_{V,t}, \quad [5]$$

where $\langle \cdot \rangle_{A,t}$ is a combined average with respect to time and full horizontal cross section A and $\langle \cdot \rangle_{V,t}$ with respect to time and full cell volume $V = AH$. The main text reports the results for Nu only (see also Table S1 and the text further below). The Reynolds number Re (and thus the turbulent momentum transfer) is given in dimensionless units by

$$\text{Re} = \tilde{u}_{\text{rms}} \sqrt{\frac{\text{Ra}}{\text{Pr}}} \quad \text{with} \quad \tilde{u}_{\text{rms}} = \langle \tilde{u}_x^2 + \tilde{u}_y^2 + \tilde{u}_z^2 \rangle_{V,t}^{1/2}. \quad [6]$$

Note that the error for Reynolds number (as given in Table 1 of the main text) was found by determining the average Reynolds number for the first and second halves of the simulation time and then finding the difference between these and the average of Reynolds number for the entire simulation time.

Numerical simulations

The equations are numerically solved by the Nek5000 spectral element method package (<https://nek5000.mcs.anl.gov>) which has been adapted to the present application and converges exponentially fast (1). All turbulent fields are therefore expanded in each space dimension and on each of the N_e spectral elements by Lagrangian interpolation polynomials of order N composed of Legendre polynomials. The three-dimensional basis is composed by a tensor product (2).

The initial conditions (ICs) were $\mathbf{u} = 0$ and $T = 1 - z$ plus small random perturbations for all cases, except for the highest two Rayleigh numbers. In the case of $\text{Ra} = 10^{14}$, we started with data from the run at $\text{Ra} = 10^{13}$ and random ICs, and then ramped this run up to the higher Rayleigh number after the $\text{Ra} = 10^{13}$ case became settled. Since this case did not use the same grid as for the production run at $\text{Ra} = 10^{13}$, we applied a spectral element remeshing (see also Table 1 in the main text). The run at $\text{Ra} = 10^{15}$ was ramped up from the settled $\text{Ra} = 10^{14}$ case.

The largest direct numerical simulations at $\text{Ra} = 10^{15}$ was conducted with 524,288 Message Passing Interface (MPI) processes on the Blue Gene/Q supercomputer Mira at the Argonne National Laboratory that alone required more than 100 million core-hours.

Comparison with cryogenic convection experiment

Figure S1 shows a comparison of the present turbulent heat transport data with selected data from past simulations (3) and experiment (4) with which one or the other of the present authors was involved. Comparisons with other sources essentially agree for $\text{Ra} < 10^{12}$ but differences occur for larger Ra . The present data are intended to give a more definitive answer to the scaling law up to $\text{Ra} = 10^{15}$. As argued in the main text, our expectation is that the smallness of the present aspect ratio is not a limitation for the heat transport results. It is worth pointing out that, after examining all possible experimental artifacts, the authors in ref. (4) concluded that the scaling exponent was approximately $1/3$.

Convergence of Nusselt number data

Figure S2 shows the typical convergence process of the Nusselt number at the plate with respect to polynomial order N . Simulations are performed in an up- and down-ramping scenario of the spectral resolution. This procedure allowed us to cover longer time periods of the large-scale flow evolution at the higher Rayleigh numbers. While the system does appear to alternate among several “barber pole” states (see Fig. 5 of the main text), especially for the lower Rayleigh numbers, no clear correlation was found between the Nusselt number and winding number. Turbulence statistics were gathered for the higher spectral resolutions only and exclude the spikes at the switching points.

The spectral element method converges exponentially fast (5) and thus requires fewer grid points inside the boundary layer in comparison to the finite difference method, as demonstrated, for example, in ref. (6). We also computed the Kolmogorov length η_K for each Rayleigh number as defined in ref. (1), and our smallest grid spacing is always smaller than the Kolmogorov length.

Table S1 compares the results obtained from both determination methods for the Nusselt number as given in Eq. (4) and Eq. (5). We found that the Nusselt number Nu_V which is determined by Eq. (5) always fluctuates more strongly than Nu which is based on Eq. (4). This is due to the large velocity fluctuations in the slender cell and the short integration times for the highest Rayleigh numbers. This is why we only report Nu in the main text.

Ra	Nu	Nu _V
10 ⁸	29.94 ± 0.04	29.94 ± 0.01
10 ⁹	58 ± 10	59 ± 5
10 ¹⁰	107 ± 11	107 ± 11
10 ¹¹	229 ± 13	222 ± 25
10 ¹²	503 ± 25	510 ± 70
10 ¹³	1,075 ± 44	806 ± 120
10 ¹⁴	2,228 ± 100	2,000 ± 200
10 ¹⁵	4,845 ± 200	4,500 ± 300

Table S1. Comparison of the Nusselt number determination by two different methods. The data in the main text are obtained from the diffusive heat flux through the top/bottom plates Nu which is calculated at $\tilde{z} = 0, 1$. Alternatively, the turbulent heat flux can be obtained by the combined average with respect to cell volume and time Nu_V which is shown in the third column of the table. This value comprises a volume-time average of the total heat flux. It is seen that the two estimates agree for almost all cases within the error bars, even for the largest Rayleigh numbers. Again, $Pr = 1$ for all simulations. See the SI text for the exact definitions of both Nusselt numbers. The error is computed from the standard deviation of the time series.

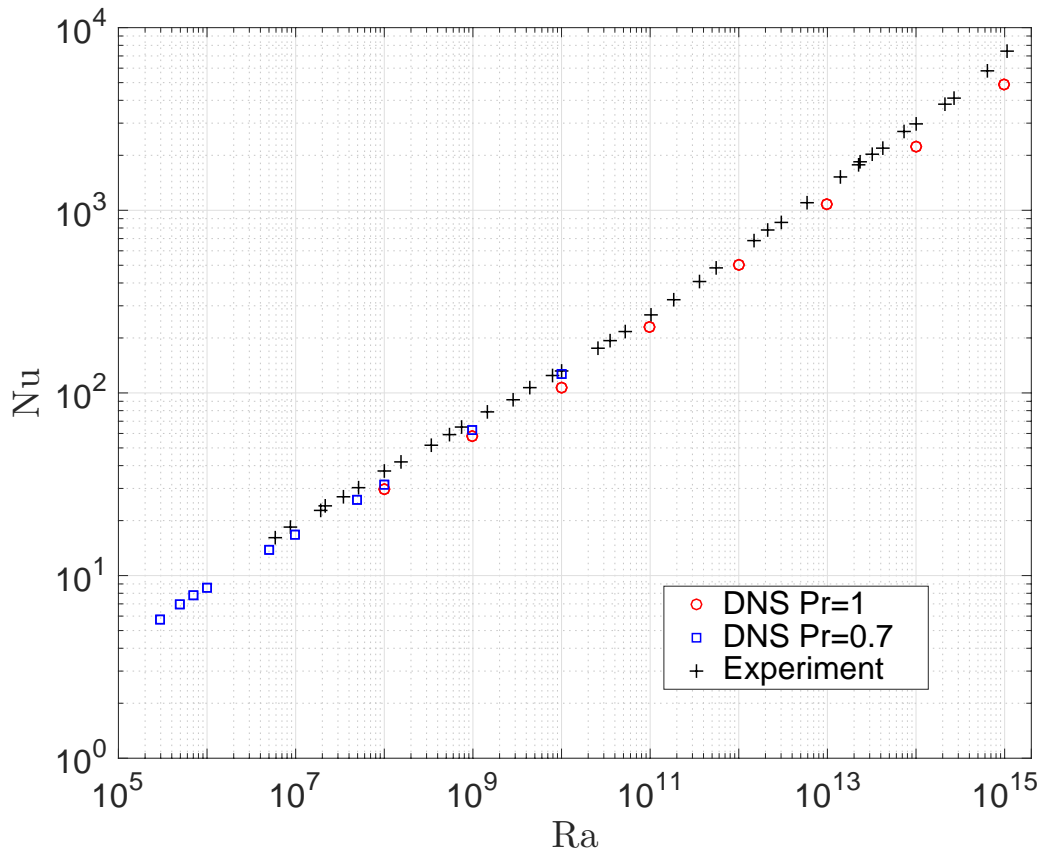


Fig. S1. Comparison of turbulent heat transfer law in simulation and experiment. Nusselt number Nu versus Rayleigh number Ra for the present simulations (open circles) at $Pr = 1$ and $\Gamma = 0.1$, previous simulations (open squares) at $Pr = 0.7$ and $\Gamma = 1$ taken from ref. (3), and experimental data in cryogenic helium (crosses) at $\Gamma = 1$ and $Pr \gtrsim 0.7$ taken from ref. (4).

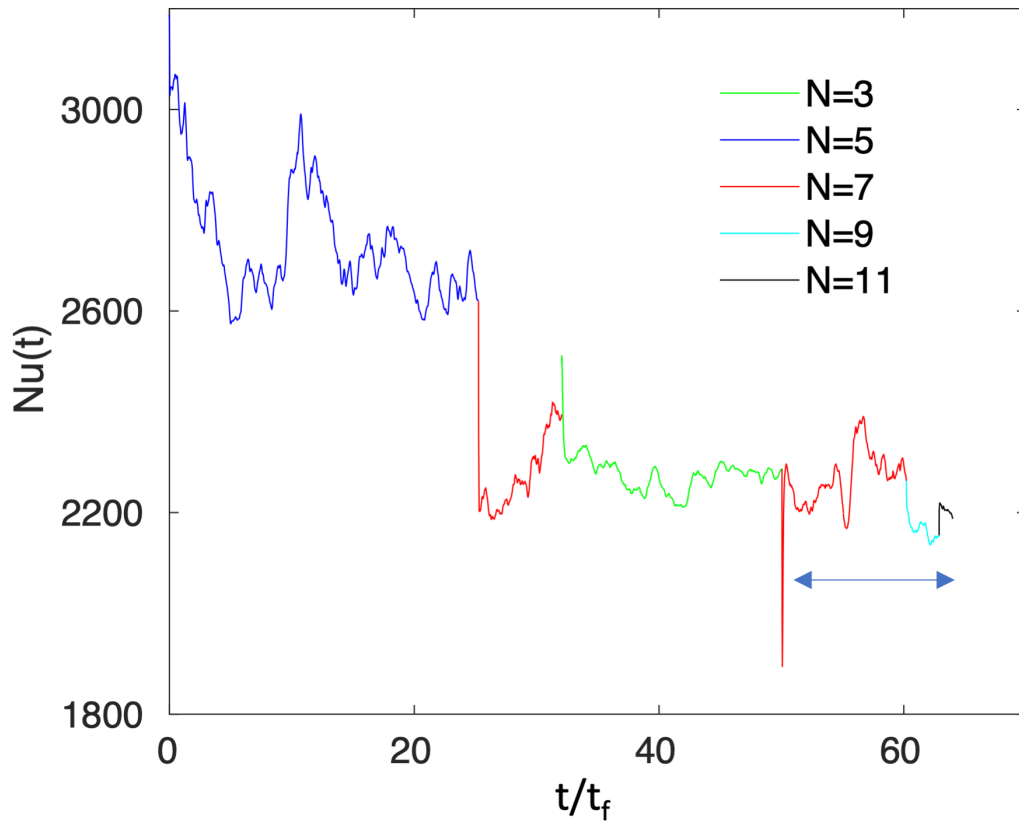


Fig. S2. Convergence of the Nusselt number Nu as a function of simulation time and the polynomial order N . Integration time is given in units of the free-fall time t_f for $Ra = 10^{14}$. The variation of Nu is displayed as the direct numerical simulations are ramped up to the maximum spectral resolution. N here is the order of the interpolating Lagrangian polynomials. The largest value of the spectral order $N = 11$ in each space direction and on each of the more than 17 million spectral elements that fill the cylindrical cell volume (see Table 1 of the main text). The data discussed in the main text have been taken from the simulations for times $t > 50t_f$ only (see arrow).

References

1. Scheel JD, Emran MS, Schumacher J (2013) Resolving the fine-scale structure in turbulent Rayleigh-Bénard convection. *New J. Phys.* 15:113063.
2. Fischer PF (1997) An overlapping Schwarz method for spectral element solution of the incompressible Navier-Stokes equations. *J. Comput. Phys.* 133:84–101.
3. Scheel JD, Schumacher J (2017) Predicting transition ranges to fully turbulent viscous boundary layers in low Prandtl number convection flows. *Phys. Rev. Fluids* 2:123501.
4. Niemela JJ, Sreenivasan KR (2003) Confined turbulent convection. *J. Fluid Mech.* 481:355–384.
5. Deville MO, Fischer PF, Mund EH (2002) *High-Order Methods for Incompressible Fluid Flow* (Cambridge University Press, Cambridge, UK).
6. Kooij GL, Botchev MA, Frederix EMA, et al. (2018) Comparison of computational codes for direct numerical simulations of turbulent Rayleigh-Bénard convection. *Comput. Fluids* 166:1–8.

Correction

In Table 1 of the main manuscript, the number of spectral elements is $N_e = 192,000$ for all four runs from $Ra = 10^8$ to 10^{11} and $M = 52$ for $Ra = 10^{14}$.